Design and Optimization of Ultrasound Phased Arrays for Large-Scale Ultrasound Neuromodulation

Sheikh Jawad Ilham, *Student Member, IEEE,* Zeinab Kashani, *Student Member, IEEE,* and Mehdi Kiani, *Senior Member, IEEE*

***Abstract*—Low-intensity transcranial focused ultrasound stimulation (tFUS), as a noninvasive neuromodulation modality, has shown to be effective in animals and even humans with improved millimeter-scale spatial resolution compared to its noninvasive counterparts. But conventional tFUS systems are built with bulky single-element ultrasound (US) transducers that must be mechanically moved to change the stimulation target. To achieve large-scale ultrasound neuromodulation (USN) within a given tissue volume, a US transducer array should electronically be driven in a beamforming fashion (known as US phased array) to steer focused ultrasound beams towards different neural targets. This paper presents the theory and design methodology of US phased arrays for USN at a large scale. For a given tissue volume and sonication frequency (*f*), the optimal geometry of a US phased array is found with an iterative design procedure that maximizes a figure of merit (FoM) and minimizes side/grating lobes (avoiding off-target stimulation). The proposed FoM provides a balance between the power efficiency and spatial resolution of a US array in USN. A design example of a US phased array has been presented for USN in a rat's brain with an optimized linear US array. In measurements, the fabricated US phased array with 16 elements (16.7×7.7×2 mm^3), driven by 150 V (peak-peak) pulses at *f* = 833.3 kHz, could generate a focused US beam with a lateral resolution of 1.6 mm and pressure output of 1.15 MPa at a focal distance of 12 mm. The capability of the US phased array in beam steering and focusing from -60^o to 60^o angles was also verified in measurements.**

***Index Terms*—Transcranial focused ultrasound stimulation, neuromodulation, ultrasound transducer, phased array, focusing, beam steering, beamforming, spatial resolution.**

I. Introduction

Low-intensity transcranial focused ultrasound stimulation (tFUS), as a noninvasive neuromodulation modality for both activation and suppression of neural activity, is very promising due to its improved spatial resolution of millimeter (mm) scale compared to its noninvasive counterparts, such as transcranial magnetic stimulation (TMS) and transcranial direct and alternating current stimulation (tDCS, tACS) [1], [2]. tFUS can be utilized in basic neuroscience research in chronic studies of animals for understanding brain function. In clinical applications, tFUS can potentially provide the promise of better treatment and prevention of different neurological and psychiatric disorders [3]-[6].

tFUS has been demonstrated successfully in a wide range of animals and even humans [7]-[14]. For example, motor responses have been evoked in mouse brains by 50 ms sonication of 80 cycles of ultrasound (US) pulses at 1.5 kHz rate (sonication frequency, *f*, of 350 kHz) with the spatial-peak pulse-average intensity (I_{sppa}) of 230 mW/cm^2 with a temperature increase of < 0.01^o C [7]. tFUS for eliciting body movements in rats from various areas (tail, limbs, whiskers, head) by delivering US to motor cortical areas at *f* of 0.6-2 MHz with I_{sppa} of ~ 10 W/cm^2 has been demonstrated [8], [9]. The activities of the primary visual and somatosensory cortex in humans have been modulated with tFUS with I_{sppa} of < 6 W/cm^2 [12]-[14]. Until now, most of these research endeavors have focused on studying the effects of US on the nervous system. Although some effects have been observed at US pressure levels as low as 100 kPa [15], hundreds of kPa US pressure (up to ~ 1 MPa) is often needed for reliable tFUS.

Conventional tFUS systems utilize bulky single-element US transducers, which are driven by off-the-shelf electronics, and suffer from multiple shortcomings [9]-[14]. 1) They can only target a fixed and limited region of the brain. To change the stimulation target, their US transducers must be mechanically moved. 2) They can operate for only several hours in constrained experimental environments. 3) They are limited to use in anesthetized animals due to the bulky apparatuses. However, an optimal technology for long-term (24/7), large-scale ultrasound neuromodulation (USN) in behaving animals (e.g., rodents) requires a miniaturized US transducer array that is electronically driven in a beamforming fashion (also known as a US phased array) to steer focused US beams towards different neural targets.

Recently, there have been some efforts to partially mitigate some of the issues in conventional tFUS systems. In [8], [16], and [17], miniature single-element US transducers, connected to the driving electronics through a cable, have been mounted

Manuscript received July 9, 2021, revised Sept. 23 and Oct. 26, 2021.

This work was supported by the National Institutes of Health (NIH) and National Science Foundation (NSF) under Grants R21EY029424 and ECCS-1942839, respectively.

S. Ilham, Z. Kashani, and M. Kiani* are with the School of Electrical Engineering and Computer Science at the Pennsylvania State University, University Park, PA 16802, USA (phone: 814-867-5753, email: mkiani@psu.edu).

*Corresponding author

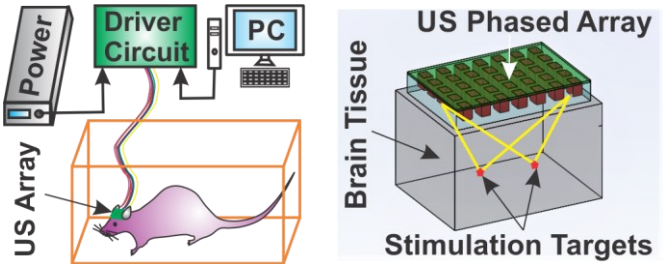

Fig. 1. Conceptual schematic of the large-scale USN in a behaving animal using a miniaturized wearable US array, electronically driven in a beamforming fashion for beam steering and focusing in a brain tissue volume.

on the rats' and mice's head, respectively. Although these systems enable longer-term studies on behaving animals, they still suffer from a fixed transmitted US beam, i.e., only a fixed stimulation site. A US phased array can be placed on either an intact skull or a brain tissue with a partially removed (or thinned) skull, as depicted in Fig. 1, to deliver focused US beams to different neural targets. Hence, USN with a broad spatial coverage can be realized thanks to beam steering.

Several US arrays have recently been reported for USN. A flexible patch with a linear (1D) 8-element piezoelectric US array (f = 1.3 MHz), generating US pressure output of 80 kPa/V, has been developed in [18] for stimulating the peripheral nervous system (PNS). A ring-shaped 32-element capacitive micromachined US transducer (CMUT) array (f = 183 kHz), generating a low US pressure output of 52 kPa (driven at 90 V), has been reported in [19]. In [20], a linear 128-element (50 mm aperture) piezoelectric US array, generating US pressure output of 930 kPa (driven at ±48 V), has been fabricated and tested on a mouse at f = 5 MHz. In [21], a 1 MHz 256-element 2D array based on a new piezoceramic with high dielectric permittivity has been presented for low-intensity US therapy applications. In [22], a 2D transmit beamformer ASIC with integrated piezoelectric transducers at 8.4 MHz has been presented in a 5 V CMOS process. But due to its low 5 V operation, this system can only generate ≤ 100 kPa US pressure outputs. A 60 V, 2D transmit beamformer CMOS ASIC with integrated CMUT array at 2 MHz has been presented in [23], achieving a peak US pressure output of ~ 575 kPa.

Despite these recent efforts, the literature still lacks a detailed design methodology for finding the optimal geometry of a US phased array for a given tissue volume and f (from the application) to achieve the highest performance in USN experiments. The US arrays in prior works have not been optimized based on a detailed methodology that considers the application and fabrication constraints. For optimal USN at a large scale using a US phased array, the highest US pressure and finest spatial resolution (at a given f) at the focal spot should simultaneously be achieved at different steering angles with minimal input electrical power (improving the power efficiency of the phased array) and attenuated undesired side/grating lobes (avoiding off-target stimulation). While the required input power is relatively high in USN and increasing f can improve the spatial resolution, a design methodology is needed to simultaneously optimize the power efficiency of an array along with the spatial resolution of its generated beam. These metrics highly rely on the design specifications of a US phased array.

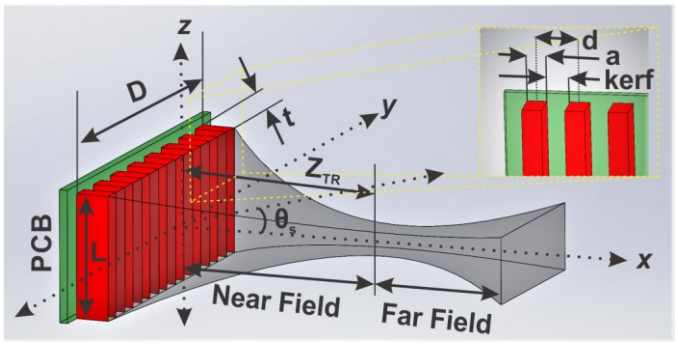

Fig. 2. A linear US phased array with a conceptual beam shape, consisting of near- and far-field zones.

The main contributions of this paper are: 1) Presenting an optimal design methodology of US phased arrays with an iterative design procedure with low computational expense for USN at a large scale; 2) Proposing a new figure of merit (FoM) that strikes a balance between the power efficiency and spatial resolution of a US array (while minimizing unwanted side/grating lobes) for optimizing US phased arrays for USN; 3) Helping the designers of USN systems optimize a US phased array as the first step towards a portable system for long-term, large-scale USN in behaving animals; And 4) validating the proposed design procedure with comprehensive experimental results. The theoretical foundation of US beam steering and focusing will be discussed in Section II, followed by the design and optimization of US phased arrays for USN in Section III. The fabrication and measurement of the optimized US phased array will be presented in Section IV, followed by the concluding remarks in Section V.

II. Theory of Ultrasound Beam Steering and Focusing

In designing large-scale USN systems with US phased arrays, it is critical to understand the theoretical foundation of US beam steering and focusing. While the basic theory has been studied in the literature [24], [25], a summary with an emphasis on key parameters in the USN context is given here. For simplicity, linear phased arrays have been optimized and characterized in this paper, but similar design methodologies can also be generalized to 2D phased arrays.

A linear phased array consists of several US transducer elements arranged in a single line assembly with identical spacing. As an example, Fig. 2 shows a linear phased array with 8 elements (N = 8), in which d is the interelement spacing (or pitch), a is the element width, L is the element length in the elevation direction, and D is the total array width (or aperture). The difference of d and a is the *kerf*. The thickness of each US element is denoted by t. In this paper, the top surface of the array is assumed to be in the yz plane (centered at the origin), having its aperture and elevation length extended along the y and z axes, respectively.

The US beam generated by a linear array (Fig. 2), while driving all its elements with the same phase, has two distinct zones: Fresnel zone (near field) and Fraunhofer zone (far field) [26]. A linear array can only be focused within the near-field region, which ends at the Rayleigh distance, $Z_{TR} = D^2/4\lambda$ (when $D >> \lambda$), where λ is the US wavelength in the medium [24]. For beam formation at a particular focal distance (F), the US

elements should be excited with a specific delay pattern so that US waves from all the elements arrive at F constructively (with the same phase). For optimal beam steering and focusing at F with the azimuthal angle θ_s (in the ***xy*** plane with respect to the normal axis ***x*** in Fig. 2), the excitation time delay (Δt_n) for the n^{th} element can be calculated from:

$$\Delta t_n = (F/c)(1 - \sqrt{[1 + (nd/F)^2 - 2ndsin(\theta_s)/F]}) + t_0 \quad (1)$$

where $c = \lambda \times f$ is the US velocity and t_0 is a common delay offset [24]. In addition to the main lobe in the steering direction θ_s, there are also side lobes in many other directions and grating lobes whose magnitudes are comparable to the main lobe.

The effect of US array parameters on its beam steering and focusing capability has been studied in [25] with some simplifications. They have defined a directivity function, $H(\theta)$, as the peak US pressure at any angle θ normalized by the peak US pressure at the steering angle θ_s:

$$H(\theta) = \left|\frac{\sin[\pi a \sin(\theta)/\lambda]}{\pi a \sin(\theta)/\lambda} \frac{\sin[(\pi d(\sin(\theta_S) - \sin(\theta))/\lambda)N]}{N \sin[(\pi d(\sin(\theta_S) - \sin(\theta))/\lambda)]}\right| \quad (2)$$

Note that $H(\theta) = 1$ at $\theta = \theta_s$, and it depends on the array geometry (a, d, N). To attenuate side/grating lobes, $H(\theta)$ should be minimized at $\theta \neq \theta_s$. Based on (2), the array directivity improves by increasing both N and d (or D) but increasing θ_s degrades the directivity. While increasing N (or D) improves both the directivity and spatial resolution, the directivity improvement is relatively less at larger N.

At large d with improved directivity, amplified side/grating lobes may be introduced. By simplifying the array to discrete line sources, the maximum d that avoids grating lobes for a given θ_s has been found in [25]:

$$d_{max} = \lambda/(1 + \sin\theta_s) \times (N - 1)/N \quad (3)$$

Therefore, d cannot be increased indefinitely. For example, with large N and $\theta_s = 90°$, d should be chosen as $d_{max} = \lambda/2$.

While the directivity of a US array is important, in USN applications several parameters need to be considered simultaneously. 1) The US pressure (P) at the focal spot should be maximized for a given input power to the array to optimize the power efficiency of the array. 2) The focal volume (V) at the focal spot should be minimized to achieve the highest possible spatial resolution (or specificity) particularly in tFUS with low f. 3) In achieving these requirements with a US phased array, any off-target stimulation due to side/grating lobes should be eliminated by improving the array directivity. Therefore, an accurate design methodology with a new FoM is needed to optimize the geometry of a US phased array for USN given the application and fabrication constraints in a realistic experimental setup.

III. Optimal Design of Ultrasound Phased Arrays for Ultrasound Neuromodulation

As introduced in Fig. 2, the geometric design parameters of a linear US phased array are d, L, a, N, D, and t. For USN applications the sonication frequency f and targeted tissue, dictating the maximum F and θ_s as well as c (or λ), are among the design parameters. Optimizing these parameters is critical for achieving the optimal performance.

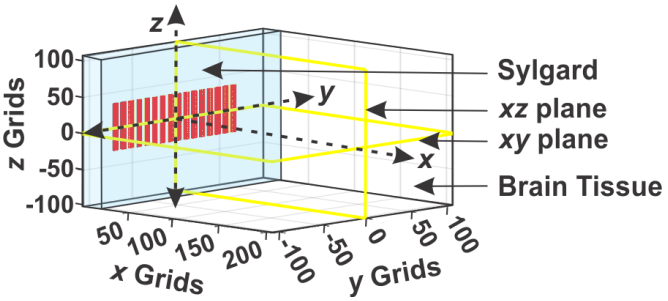

Fig. 3. k-Wave simulation setup used to optimize a US phased array. The array surface is parallel to the ***yz*** plane and centered at the origin ***x*** = ***y*** = ***z*** = 0. Both the ***xy*** and ***xz*** planes were defined as sensors for recording US pressure.

While equations (1)-(3) can be used to find the initial values of the array geometry, further optimization is needed in an accurate simulation tool, such as k-Wave toolbox in MATLAB (MathWorks R2019b, Natick, MA), which can also model US propagating media. k-Wave can numerically calculate the resultant acoustic field radiated from multiple sources by solving a set of coupled first-order wave equations [27], and its accuracy has experimentally been validated [28].

Fig. 3 shows our US array setup in k-Wave, in which the array surface is parallel to the ***yz*** plane and centered at the origin (***x*** = ***y*** = ***z*** = 0). The ***xy*** and ***xz*** planes are defined as sensors for recording US pressure. A 216×216×216 grid space with 130 µm resolution is defined such that the first 12 ***yz*** planes (thickness of ~ 1.5 mm) from the array surface and beyond that (204 planes) have acoustic properties of sylgard-184 (Dow Inc., Midland, MI) and brain tissue, respectively. The temporal acoustic wave propagation is simulated for ~ 29.7 µs with 1190 steps of ~ 25 ns. To model the boundary condition, a 0.65 mm thick perfect matching layer (PML) is added at the boundaries of the medium. The sound speed in (and mass density of) the brain tissue and sylgard-184 are set to 1560 m/s (1040 kg/m^3) and 1030 m/s (1050 kg/m^3), respectively [29], [30]. To mimic the brain tissue in simulations, the power-law pre-factor, power-law exponent, and the nonlinearity parameter are set to 0.6 dB/(MHz.cm), 1.5, and 7.1, respectively [30]. With these settings, each simulation is completed in ~ 35 min on average using a standard desktop with a core i7 CPU (3.4 GHz) and 16 GB of RAM. For the same condition, the simulation time is almost doubled for a 2D array (16×16-element).

All design parameters of an array can be simulated in k-Wave, except the US element thickness (t) that determines the thickness-mode resonance frequency [26]. Similar to our work in [17], COMSOL Multiphysics (COMSOL, Inc., Bulington, MA) is used to simulate a single US element and find the optimal t for operation at a desired f.

A. Figure of Merit (FoM) for Optimizing Phased Arrays for Ultrasound Neuromodulation

For optimizing phased arrays for USN, we define $FoM = P/(\sqrt{NaL} \times \sqrt[3]{V})$, where P and V represent the spatial peak US pressure output (for the same voltage amplitude across each element) and half-power-beam-width (HPBW) focal volume at the focal spot, respectively. As the pressure source of each element is defined with uniformly distributed point sources

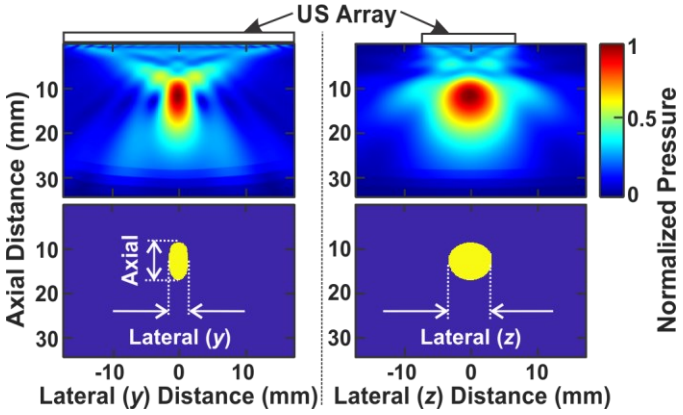

Fig. 4. Acoustic beam profiles (normalized US pressure output) of a 16-element array in the (a) ***xy*** and (b) ***xz*** planes (Fig. 3) for calculating FoM.

over a defined source mask in k-Wave, by increasing $N \times a \times L$, which is the total piezoelectric area, the input electrical power to the array is also increased. Since the US pressure squared (P^2) is proportional to the input power, the term $P/\sqrt{NaL}$ is considered in the FoM to ensure a constant total input power to the array as N, a, and L change in the optimization. Therefore, this FoM provides a balance between the power efficiency and spatial resolution of a US array.

To clarify the FoM calculation, Figs. 4a and 4b show the acoustic beam profiles (normalized US pressure output) of a 16-element array in the ***xy*** and ***xz*** planes (Fig. 3), respectively. The absolute maximum US pressure output at the focal spot is called P. Since k-Wave can only provide the focal gain (i.e., absolute pressure values depend on initial pressure distributions in k-Wave), the simulated US pressure outputs are all normalized to one in this paper. Therefore, the absolute values of FoM are not important in the optimization. Indeed, the design that provides relatively the highest FoM is the optimal one.

In Fig. 4, lateral (parallel to array; ***y*** and ***z*** directions) and axial (normal to array; ***x*** direction) resolutions are defined as the beam width, at which the US intensity reduces to half (-3 dB) or US pressure reduces by ~1.4-fold [7]. From identified lateral and axial resolutions, the HPBW focal volume V can be calculated by integrating the highlighted area in the ***xy*** plane (Fig. 4a) and multiplying it by the lateral resolution in the ***z*** direction (Fig. 4b). For simplicity in computations, the worst-case (largest) lateral resolution in the ***z*** direction is considered in calculating V, and FoM is calculated at a θ_s of 0° in k-Wave simulations. This only maximizes the generated US pressure for a given input power, and therefore, one should apply a proper voltage to the array to achieve the required US pressure for successful USN at different θ_s [31].

To consider the side/grating lobes in array optimization, the directivity function can be used. Since $H(\theta)$ in (2) has been found with simplified assumptions, k-Wave simulations are used to find the directivity accurately. For simple calculations in k-Wave, a comparable directivity function, $H(y)$, is proposed as the ratio of the peak US pressure output along the lines parallel to the ***x*** axis at each ***y*** ($z = 0$; Fig. 3) to the peak US pressure output at the focal spot. Therefore, both $H(\theta)$ and $H(y)$ represent the largest US pressure outside the focal spot in the ***xy*** plane only at different axes (θ vs. ***y***). Note that $H(y) = 1$ at the ***y*** corresponding to the focal spot. As the beam width is defined by half power (equivalent to ~ 0.7 of peak pressure), a calculated $H(y) < 0.7$ away from the focal spot would be sufficient. Due to nonidealities, $H(y) < 0.5$ is considered in our optimization (one can use smaller values).

B. Ultrasound Phased Array Design Procedure

A design procedure is presented in Fig. 5 to maximize the proposed FoM and minimize side/grating lobes with $H(y) < 0.5$ of a US phased array for USN by optimizing the array geometry (d, L, a, N, D, t in Fig. 2). The optimization flowchart starts with the design constraints imposed by the application, including 1) the maximum focal distance (F_{max}), maximum steering angle ($\theta_{s,max}$), maximum array size (D_{max} and L_{max}), and sound speed (c) dictated by animal/human subject (as for example animal's head/brain size [32]) and its targeted tissue, 2) desired sonication frequency f, and possibly 3) the maximum number of elements (N_{max}) limited by driving electronics. Also, design constraints imposed by the fabrication limitations, such as the minimum *kerf* limited by the blade thickness of a saw machine, are included in step 1.

Some of these parameters are related as $a \le d$ - *kerf*, $\lambda = c/f$, $F < D^2/4\lambda$, and $N \times d$ - *kerf* = D. Therefore, they can affect each other in the optimization. Based on $F < D^2/4\lambda$, D (and N) should be large enough for a given f (or λ) to achieve beamforming at F_{max}. Otherwise, one should increase f (decrease λ) for the proper operation of a phased array. Increasing f reduces the required t in the piezoelectric element for operating in the thickness-mode resonance. Therefore, one should consider the fabrication limitations of piezoelectric elements with very small t. For driving US arrays with large N, CMOS ASICs can be developed with high channel counts [33]. Thus, it is recommended that the array geometry is optimized based on D_{max}, and driving electronics are then developed with optimal N channels. But if the US array is to be driven by available electronics with limited N, one should also consider N_{max} in the optimization. It is worth noting that L, a, and d are the independent sweeping parameters, whereas N and D are dependent on d with the relation of $D = N \times d - kerf$.

In step 2, the initial values for d, N, D, and a are chosen. Based on (3) at large N and θ_s, d should be ~ $\lambda/2$, which is chosen as the initial value for d. If N is limited, N_{max} is chosen and the initial value for $D = N \times d$ - *kerf* is calculated, which should be less than D_{max}. If calculated $D > D_{max}$ or N is not limited, D_{max} is chosen as the initial value. Then, the initial value for N is calculated from $D_{max} = N \times d$ - *kerf*. To provide room for sweeping d, the initial value for a is chosen as $d/2$.

In step 3, the array geometry (L, d, a) is optimized. To reduce the computational time of the optimization, L is first swept independently, while d and a (their sweeping range depend on each other) are swept together with a sub-optimal L. In step 3.1, L is swept to maximize the FoM at F_{max} and $\theta_s = 0°$. Using the L value with the highest FoM, in step 3.2 both d and a are swept, in which at each d the new N is calculated from $D_{max} = N \times d$ - *kerf* (note $N \le N_{max}$ if given) and the upper limit for a is d - *kerf*. This leads to a 3D plot for FoM vs. d and a at F_{max} and $\theta_s = 0°$.

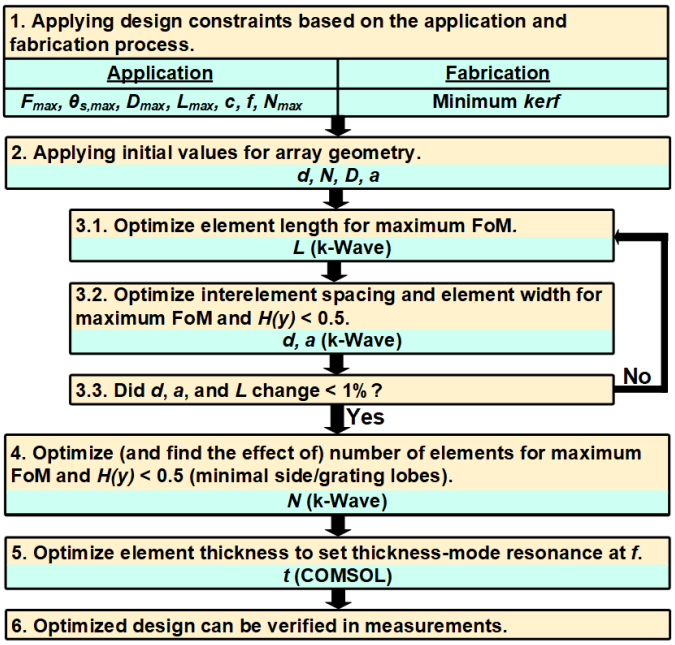

Fig. 5. Iterative optimization flowchart for designing US phased arrays for USN applications using k-Wave and COMSOL simulations.

To minimize side/grating lobes, $H(y)$ at F_{max} and $\theta_{s,max}$ (worst-case scenario) at different d values is also calculated using the corresponding a values that maximized the FoM. The d and a that lead to the maximum FoM with $H(y) < 0.5$ away from the focal spot are chosen in this step. Steps 3.1 and 3.2 are repeated iteratively until d, a, and L change less than 1% in step 3.3. This results in the optimal values for d, a, and L.

Along with the optimization of d in step 3, N is also swept based on D_{max}, which most likely results in optimal N. But one should still sweep (decrease) N in step 4 to verify/find optimal N. Also, the optimal array from step 3 can possibly have too many elements (large N and D). Reducing N (or D) can minimize the bulkiness, power, complexity, and cost of the array and its driving electronics likely at the cost of lower FoM and amplified side/grating lobes. If this is acceptable to the designer, step 4 can also elucidate the effect of N on FoM and $H(y)$. Using a, L, and d values from the previous steps, N is decreased and FoM and $H(y)$ are calculated in step 4. The smallest N (N_{min}) that still results in $H(y) < 0.5$ at $\theta_{s,max}$ is the lower bound for N. The designer can choose either the optimal N (highest FoM) or any $N > N_{min}$ with the knowledge of decreased FoM. For instance, if FoM reduces slightly by decreasing optimal N, selecting a smaller N is preferable.

In step 5, a single US element is modeled in COMSOL using the optimized a and L from k-Wave, and the element thickness t is swept to set its thickness-mode resonance at the desired f. To consider the effect of the substrate, on which the array is fabricated, it should also be modeled in COMSOL simulations, similar to our work in [34]. This step determines the most optimal values for the array geometry (D, N, L, a, d, t) to achieve the highest FoM and $H(y) < 0.5$ (minimal side/grating lobes), which can be further validated and fine-tuned through measurements. It is worth noting that if an application provides a range for f, the design procedure in Fig. 5 can be repeated at different frequencies. Then the frequency (f) and array geometries that lead to the highest FoM are chosen as the optimal design.

C. Ultrasound Phased Array Design Example for Ultrasound Neuromodulation of the Rat's Brain

Based on the design procedure in Fig. 5, a US phased array (Fig. 3) was optimized for USN of the rat's brain with high FoM and $H(y) < 0.5$. For the design example, the following assumptions were made in k-Wave simulations: 1) D and L are constrained by the average size of a rat's head ($D_{max} = L_{max} = 25$ mm) [32]; 2) F is set by the average depth of a rat's brain ($F_{max} = 12$ mm), considering the thickness of the scalp and skull [35]; 3) For transcranial US transmission with low loss, f is considered < 1 MHz in tFUS applications [36] that led us to choose $f = 750$ kHz; 4) $\theta_{s,max}$ is considered as ±60°; Finally, 5) minimum *kerf* of 130 µm (one grid point). Also, a 1.5 mm-thick layer of sylgard-184 was considered on the array surface for electrical isolation and protection. For the COMSOL simulations, it was assumed that the US element is made of PZT-5A (APC Int., Mackeyville, PA), fabricated on a printed circuit board (PCB).

Fig. 6 shows geometry optimization of the array to maximize the FoM at $F = 12$ mm and $\theta_s = 0°$, and limit $H(y) < 0.5$ at $\theta_s = 60°$. Fig. 6a shows the normalized FoM vs. L assuming the initial values of $d = 1.04$ mm ($\lambda/2$) and $a = d/2 = 0.52$ mm. For small L, as L increases the peak US pressure at the focal spot slightly increases and the beam width in the z direction slightly reduces that in turn improves FoM. However, when L is too large, the beam width in the z direction starts to increase, which reduces the FoM. Therefore, the highest FoM was achieved at $L = 7.8$ mm, which was used to sweep d and a. The FoM at $L = 7.8$ mm is 18% and 30% higher compared to the FoM at $L = 5.2$ mm and 10.4 mm, respectively, indicating the effectiveness of the FoM in optimizing L.

Fig. 6b shows the 3D plot for FoM vs. d and a. For each $d < 2.08$ mm, the FoM monotonically improves by increasing a, but the highest FoM is achieved at an optimum value of a for any $d \geq 2.08$ mm. Fig. 6b also shows that for a given a, FoM increases by decreasing d as N is increased. Consequently, the maximum FoM occurred at $d = 0.78$ mm and $a = 0.65$ mm in Fig. 6b. These optimum d and a values lead to 1.8% and 14% higher FoM compared to $d = 1.04$ mm ($\lambda/2$) and $d = 1.56$ mm ($3\lambda/4$) with largest possible a, respectively, indicating the effectiveness of the FoM in optimizing d and a.

Since large d can introduce side/grating lobes, Fig. 6c shows $H(y)$ curves for different d using the corresponding a value in Fig. 6b with the highest FoM (when focusing the beam at $F = 12$ mm and $\theta_{s,max} = 60°$). It can be seen that a larger d led to higher $H(y)$ values away from the focal spot. In particular, amplified side lobes can be observed at negative θ_s ($y < 0$) at large d, as expected by the theory. Note that in calculating $H(y)$ the peak US pressure at each y can potentially happen at different axial distances. To achieve $H(y) < 0.5$, $d = 0.78$ mm (and $a = 0.65$ mm) was selected for the next iteration. The optimization led to optimal $L = 7.8$ mm, $d = 0.78$ mm, $a = 0.65$ mm, and $N = 32$. Fig. 6c shows the effectiveness of the proposed design procedure and $H(y)$ in reducing undesired side and

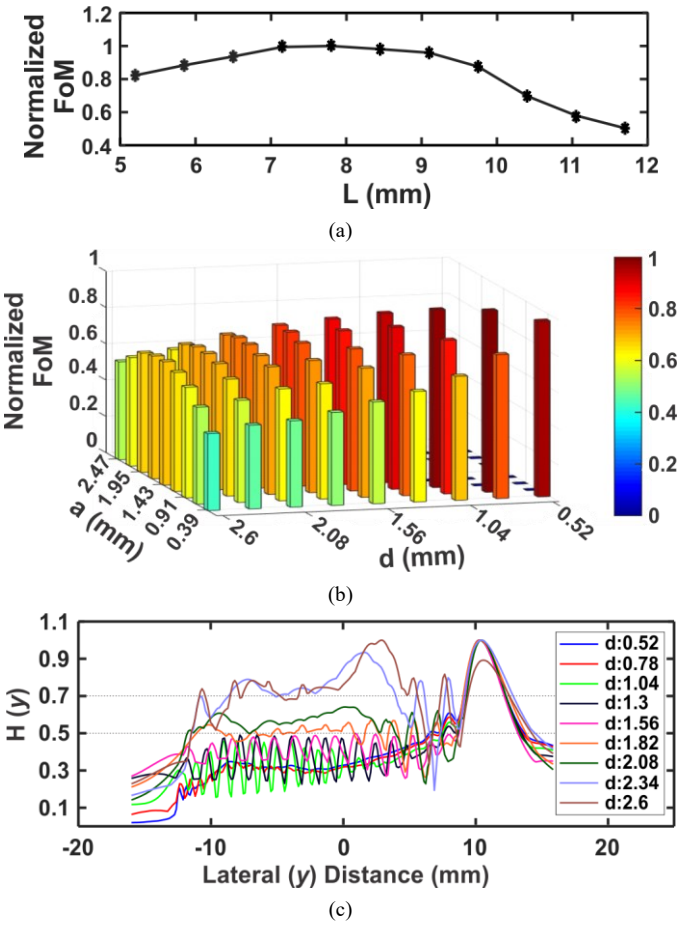

Fig. 6. Geometry optimization of the array to maximize the FoM at F = 12 mm and θ_s = 0°, and limit $H(y)$ < 0.5 at θ_s = 60°. (a) Normalized FoM vs. L with initial d = 1.04 mm and a = 0.52 mm. (b) FoM vs. d and a with L = 7.8 mm. (c) $H(y)$ at different d using the a values, which maximized FoM.

grating lobes.

Fig. 7a shows the effect of N on the FoM using optimal L, d, and a values. Intentionally, FoM was simulated for N > 32 (resulting in $D > D_{max}$) to show that 1) beyond a certain N (50 in Fig. 7a) the improvement in FoM is incremental and choosing a lower N can relax the electronics design requirements; and 2) without D_{max} limitation, there is an optimal N that maximizes the FoM. As N increases, the focal spot size reduces (and pressure increases to some extent), which improves FoM. However, at very large N the US pressure of the additional far elements contribute minimally to the focal spot pressure (while consuming more input power) due to the medium loss, thereby the FoM starts to reduce.

Finally, as shown from the impedance profile in Fig. 7b, COMSOL simulations were performed to optimize t of the 7.8×0.65 mm^2 bar-shaped US element. To resonate at f = 750 kHz, the optimal t was 2 mm. Table I summarizes the results of the optimization procedure (the array designated by "optimal US array").

Fig. 8 shows the simulated acoustic beam profiles of the optimal phased array for beam steering and focusing at F = 12 mm with θ_s of -60° to 60°. At θ_s = 0°, the simulated axial and lateral resolutions were 5.8 mm and 1 mm, respectively. To show the significance of the optimization with the proposed FoM, a US phased array with initial geometries of L = 5.2 mm, d =1.04 mm, and a = 0.52 mm was also simulated. The optimized array achieved ~ 56% higher FoM with much smaller side lobes, compared with the initial array.

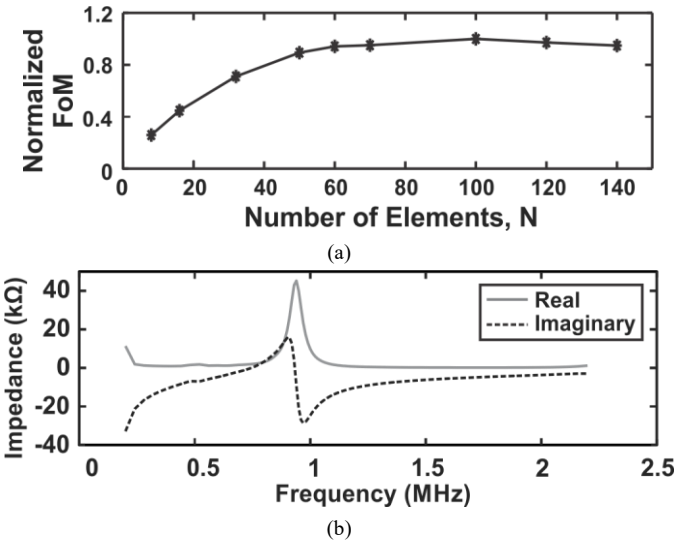

Fig. 7. (a) Normalized FoM vs. N using the optimal L, d, and a values in Table I. (b) Simulated (COMSOL) impedance profile of the 7.8×0.65 mm^2 bar-shaped US element vs. frequency to optimize t.

TABLE I
OPTIMIZED US PHASED ARRAY SPECIFICATIONS

Parameters	Optimal US Array	Measurement US Array
Sonication Frequency, f (kHz)	750	833.3
Maximum Focal Distance, F (mm)	12	12
Number of US Elements, N	32	16
US Array Aperture, D (mm)	24.8	~ 16.7
US Element Length, L (mm)	7.8	~ 7.7
US Element Width, a (mm)	0.65	~ 0.83
US Interelement Spacing, d (mm)	0.78	~ 1.06
Steering Angle, θ_s (deg)	±60	±60
Kerf, *kerf* (μm)	130	~ 230
US Element Thickness, t (mm)	2	2

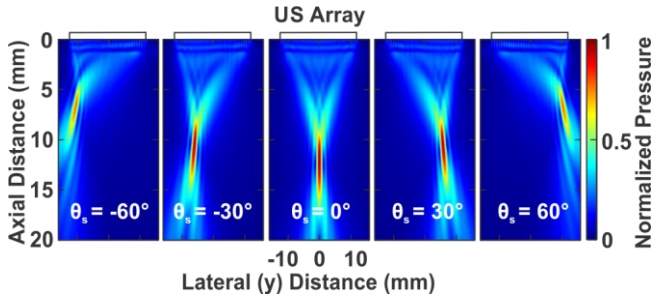

Fig. 8. Simulated acoustic beam profiles of the optimal array (Table I) for beam steering and focusing at F = 12 mm and different θ_s of -60° to 60°.

IV. ULTRASOUND PHASED ARRAY FABRICATION AND CHARACTERIZATION

In this paper, the commercially available TX7316EVM evaluation board (Texas Instruments, Dallas, TX) with limited 16 channels of high-voltage drivers (up to 200 V) was available to us for characterizing the array. The board provides a delay range of 0-40 μs with 5 ns resolution, with which θ_s of much smaller than 1° can theoretically be achieved based on (1). This is sufficient for USN applications. Therefore, to validate our

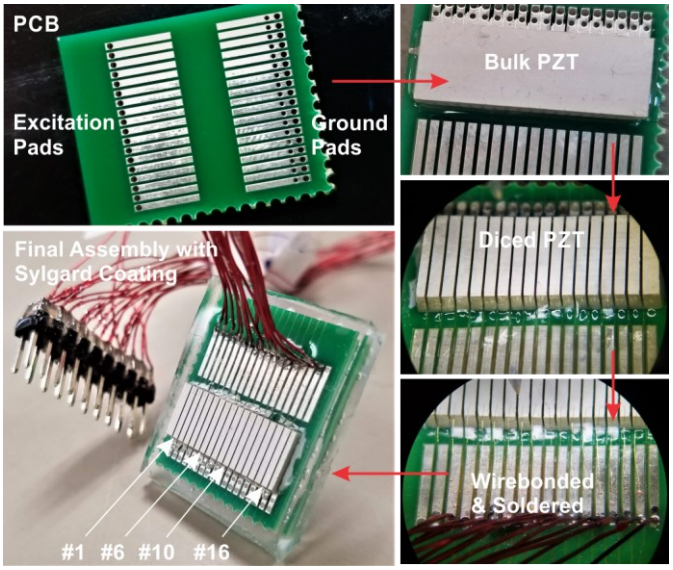

Fig. 9. The fabrication process of the US array starting from a PCB and bulk PZT plate. The final device is coated with a layer of sylgard-184.

optimization procedure in Fig. 5, only 16 elements of the US phased array was fabricated ($N = 16$) for measurement purposes (designated by "measurement US array" in Table I). To increase the array aperture with lower N of 16, d was increased to ~ 1.06 mm, which provided the second best FoM in Fig. 6b. Also, our fabrication facility could handle a minimum *kerf* of 230 µm, which could further be reduced to 130 µm, as in our optimal design, using a more advanced facility. Our k-Wave simulations show that the optimal array in Table I with $N = 32$ at $f = 750$ kHz can achieve ~ 22.1% higher FoM than the array used in measurements with smaller $N = 16$ at slightly higher $f = 833.33$ kHz. The lower FoM of the fabricated array is partly due to its smaller size (D = 16.7 mm, N = 16). Nonetheless, our measurement results in this section are mainly aimed at demonstrating the accuracy of k-Wave simulations, which are used to optimize the array.

A. Ultrasound Array Fabrication and Assembly

The 16-element array was fabricated following the steps in Fig. 9. A 2 mm thick rectangular bulk PZT-5A was cut into an 18.6×7.7 mm^2 plate. A PCB was fabricated with two rows of 18 separate excitation pads and 18 interconnected ground pads, separated by ~ 5 mm. The ground pads were covered with a layer of conductive silver paint (Leitsilber 200, Ted Pella Inc., Redding, CA) for electrical connection. The PZT plate was placed on the PCB such that ~ 4 mm length of PZT was on the ground pads, while the remaining ~ 3.7 mm PZT length located within the gap between the pads. For mechanical reinforcement during dicing, the gap was filled with Krazy Glue. Using a dicing machine with a ~ 230 µm thick saw blade, the PZT plate was diced into 18 elements with an element width of ~ 0.83 mm. Discarding the two dummy elements on the edges (added for fabrication imperfections), the top plates of the main 16 elements were wire bonded to their corresponding excitation pads. For the electrical isolation and protection of the wire-bonds, a layer of sylgard-184 was coated on the assembled device. The fabricated 16-element array size is $D \times L \times t$ = 16.7×7.7×2 mm^3.

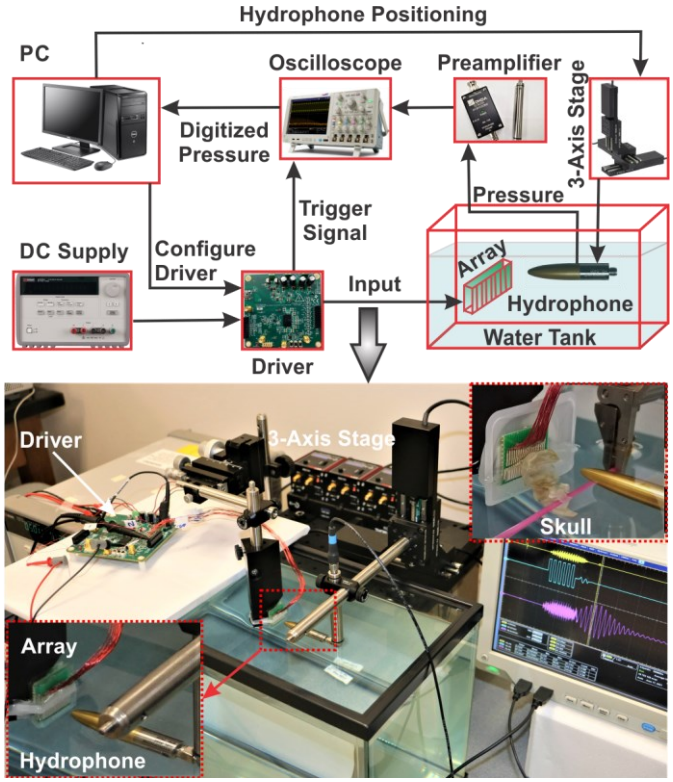

Fig. 10. Measurement setup used to measure the acoustic pressure output generated by the US phased array in a water tank (some measurements with a rat skull and tissue was also performed as detailed in Section IV.D).

B. Measurement Setup

Fig. 10 shows our custom setup for measuring the US pressure output generated by the phased array in a water tank without (Section IV.C) and with a rat skull and tissue (Section IV.D). A 3-axis translational stage, consisting of three motorized linear stages (MTS50/M-Z8, Thorlabs, Newton, NJ) with a moving range of 5 cm (0.8 µm resolution) in each axis, scans the calibrated HGL0085 hydrophone (Onda Corp., Sunnyvale, CA) with 85 µm aperture size and 0.25-40 MHz bandwidth. For recording the US pressure output, the hydrophone is connected to a digital oscilloscope (with 50 Ω termination) via the Onda AG-2010 preamplifier, providing ~ 20 dB voltage gain. A custom MATLAB script coordinates the hydrophone movement and data acquisition. After each movement, there is a 1.5 s pause before data acquisition, followed by another 1.5 s pause before the next movement. This 1.5 s pause was intentionally added for reliable data collection.

The driver board was used to drive the array without any external matching network. Six pulses (spaced by 1/f) with the optimal delay are generated every 1 ms at each channel for any beamforming scenario. A sync enable pulse from the driver board is used to trigger the oscilloscope. The stored data are post processed to filter unwanted electrical interference and plot intended acoustic beam profiles. For converting the hydrophone voltage into US pressure level, a pressure sensitivity of 52.2 nV/Pa is used based on the manufacturer calibration data. All the reported pressure values in this paper are positive pressure.

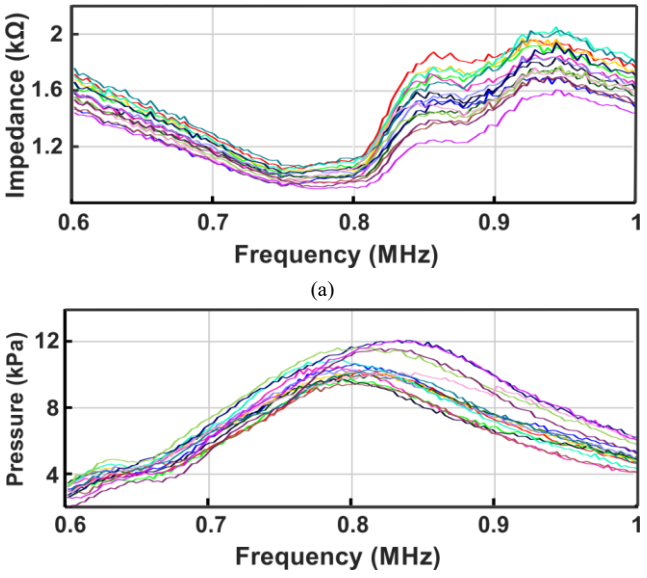

Fig. 11. (a) Measured impedance and (b) measured US pressure output at 12 mm distance (20 V peak-peak sinusoids) of all 16 channels in the fabricated US array (Fig. 7) at a frequency range of 0.6-1 MHz.

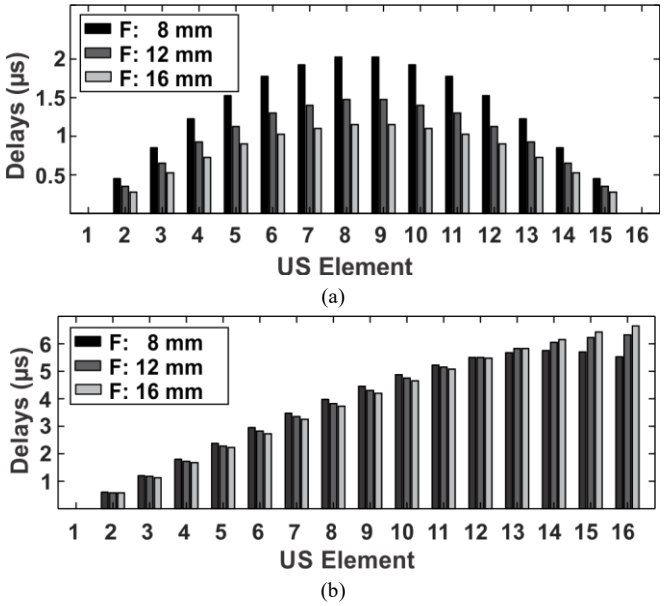

Fig. 12. Optimal delay of each element for beam steering and focusing at (a) θ_s = 0° and (b) θ_s = 45° at different focal distances F.

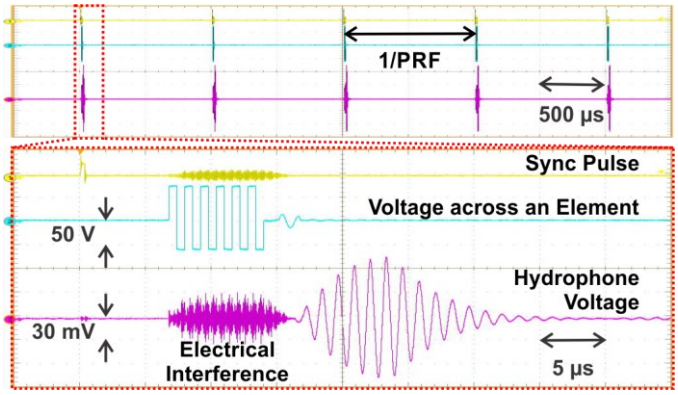

Fig. 13. Measured periodic bursts of pulses (PRF = 1 kHz) and hydrophone voltage in beam focusing at F = 12 mm (θ_s = 0°) with all 16 elements.

C. *Measurement Results*

The operation of each fabricated US element was first verified by measuring its impedance and US pressure output at a frequency range of 0.6-1 MHz. Fig. 11a shows the measured impedance of all 16 elements using a network analyzer. The series resonance frequencies are within the range of 0.75-0.8 MHz for all elements. Fig. 11b shows the measured peak US pressure outputs of 16 elements at 12 mm distance from their respective centers, while driving the elements individually with 20 V peak-peak sinusoids. The maximum, minimum, and average pressure outputs were 12.1 kPa, 9.5 kPa, and 10.6 kPa, respectively. On average, the maximum pressure output was achieved at f = 833.3 kHz, which was fixed in the rest of measurements.

The variations of impedance and pressure output among 16 elements could be due to fabrication, assembly, and measurement imperfections, including any mismatch in 1) dimensions (e.g., differences in a due to the dicing inaccuracy), 2) boundary conditions imposed by nonuniform application of glue and silver epoxy for mechanical reinforcement and attachment, 3) back-side and front-side mechanical loading likely due to nonuniform silver epoxy and sylgard-184 layers, and 4) aligning each element with the hydrophone. To quantify the effect of element-element pressure output variations, different initial pressures (consistent with Fig. 11b) were applied on 16 elements in k-Wave simulations. The simulated US beam profiles at θ_s of 0° and 45° showed minimal difference in the spatial resolution and < 20% reduction in the pressure output at the focal spot.

Beamforming (and beam steering) with the fabricated 16-element array was implemented using the driver board with 3-level square pulses. The optimal delay Δt_n for each element at different F and θ_s were found from (1), which has been implemented in k-Wave. Figs. 12a and 12b show the optimal delay of each element for beam steering at θ_s = 0° and 45°, respectively, at different F of 8 mm, 12 mm, and 16 mm. As expected, for focusing along the normal axis (θ_s = 0°), Δt_n values follow a symmetric spherical pattern with the largest Δt_n for the element(s) at the center (# 8 and 9 in Fig. 12a). Also, smaller F requires more curvature of the delay pattern. By contrast, for steering a focused beam at θ_s = 45°, Δt_n values follow a tapered spherical pattern (Fig. 12b).

Our setup can generate focused beams with stimulation patterns required for USN [7]. The driver board can operate in a burst mode with a pulse repetition frequency (PRF). Fig. 13 shows periodic bursts of pulses at PRF = 1 kHz across one of the elements, while focusing at F = 12 mm (θ_s = 0°) with all 16 elements of the fabricated array. The Fig. 13 inset shows zoomed waveforms of the sync pulse, 6 cycles of 3-level square pulses (150 $V_{p\text{-}p}$) across one element, and the hydrophone voltage corresponding to a spatial peak pressure output of ~ 1.15 MPa. To decouple the electrical interference from the hydrophone output, only 6 cycles were used in all measurements, resulting in > 95% of the achievable peak pressure with more cycles.

Several measurements were also performed to demonstrate the beam steering and focusing capability of the 16-element

TABLE II
SUMMARY OF MEASURED AND SIMULATED RESULTS OF THE FABRICATED ARRAY

Sim / Meas	Medium	Focal Dis., F (mm)	Steering Angle, θ_s (deg)	Axial Res. (mm)	Lateral (y) Res. (mm)	Lateral (z) Res. (mm)	*Peak US Pressure (MPa)	US Intensity, I_{SPPA} (W/cm^2)
Sim	Brain Tissue	12	0	8.32	1.43	3	1	-
Meas	Water			9	1.6	3.4	1.15	32.1
Sim	Brain Tissue	12	45	9	1.9	-	0.8	-
Meas	Water			11.2	1.7	-	0.99	25.9
Sim	Brain Tissue	12	-45	9	1.9	-	0.8	-
Meas	Water			11.1	1.8	-	0.94	22.3
Sim	Brain Tissue	8	0	4.6	0.98	2.9	1.1	-
Meas	Water			4.6	1	-	1.63	65.9
Sim	Brain Tissue	8	45	5.9	1.2	-	0.9	-
Meas	Water			4.6	1.1	-	1.59	62.3
Sim	Brain Tissue	16	0	11.4	1.69	3.5	0.88	-
Meas	Water			10.4	2	-	1	24.9
Sim	Brain Tissue	16	45	12.79	1.93	-	0.7	-
Meas	Water			12.8	2	-	0.92	22
Meas (yz)	With Tissue	12	0	-	1.4	3.4	1	24.9
Meas	With Skull	16	0	7.2	1.6		0.84	18.8
Meas	With Skull	16	45	6.5	1.5	-	0.76	14.9

*Simulated values for peak US pressure are all normalized to that of F = 12 mm, θ_s = 0°.

array with 150 $V_{p\text{-}p}$ pulses (and validate simulation results). Table II summarizes the measured and simulated results of the fabricated 16-element array, including the axial (***x***) and lateral (***y*** and ***z***) resolutions, peak US pressure, and corresponding I_{SPPA} when the beam was focused at different F and θ_s. These results have been described in detail in the following figures.

Figs. 14a and 14b show the simulated/measured acoustic beam profiles of the array on ***xy*** and ***xz*** planes, respectively, for beam focusing at nominal F = 12 mm and θ_s = 0°. The simulated and measured axial, lateral (***y***), lateral (***z***) resolutions were 8.32, 1.43, 3 mm and 9, 1.6, 3.4 mm, respectively. There is a good match between simulated and measured results, implying the accuracy of k-Wave simulations. Fig.14c shows measured results for beam steering at θ_s = -45° and 45° (F = 12 mm). The measured spatial peak pressure outputs were 1.14 MPa, 0.99 MPa, and 0.94 MPa at θ_s = 0°, 45°, and -45°, respectively. No grating lobes were observed in these measurements.

Fig. 15a shows measured acoustic beam profiles at F = 8 mm (within optimized F_{max} = 12 mm) with θ_s = 0° and 45°. The axial and lateral (***y***) resolutions and peak pressure output were 4.6 mm, 1 mm, 1.63 MPa at θ_s = 0° and 4.6 mm, 1.1 mm, 1.59 MPa at θ_s = 45°, respectively. The acoustic beam profile was also measured for beam steering and focusing at F = 16 mm (beyond optimized F_{max} = 12 mm) with θ_s = 0° and 45°. As expected, the peak pressure output was reduced to 1 MPa (θ_s = 0°), while axial and lateral resolutions were degraded to 10.4 mm and 2 mm (θ_s = 0°), respectively. It is likely that the sidelobes appeared in both F = 12 mm and 16 mm beam profiles are due to element-to-element pressure variations, shown in Fig. 11b.

It is worth noting that in our measurements the hydrophone was always aligned with the normal axis (***x*** in Fig. 3). Thus, the lower peak pressure output at θ_s = 45° (compared to that of θ_s = 0°) could partly be due to the directivity response of the hydrophone. For example, HGL0085 can only receive ~ 80% and ~ 70% of the generated US pressure at 45° and 60° angles, respectively. The slight tilt of the measured beams at θ_s = 0° in Figs. 14 and 15 is due to the slight angular misalignment of the array with the hydrophone, which cannot be perfectly aligned

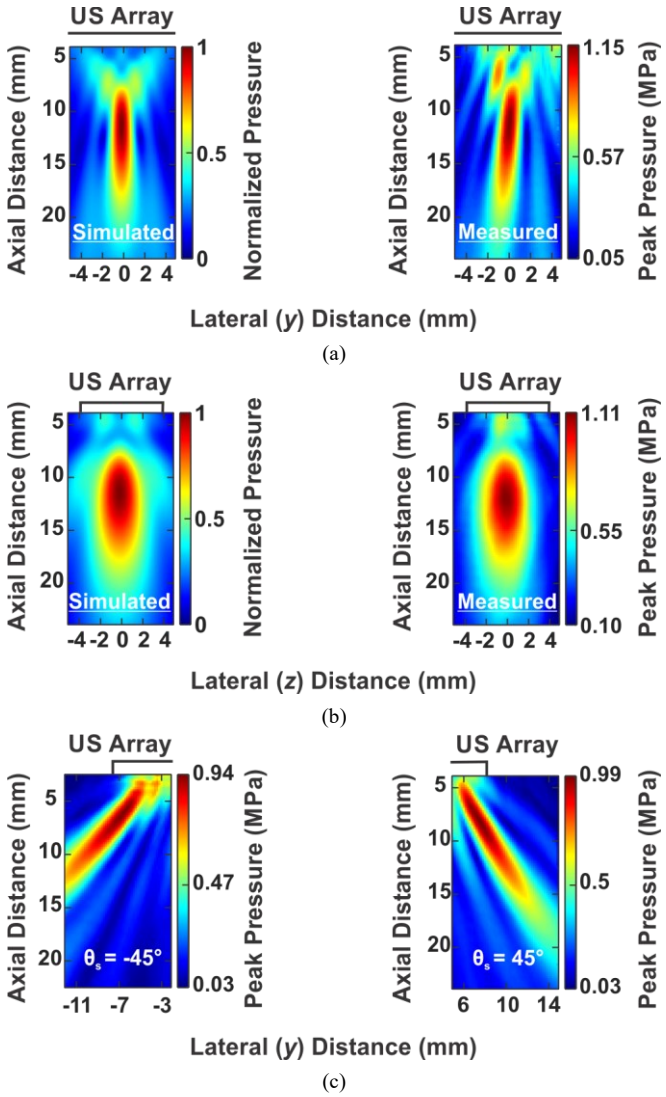

Fig. 14. Measured and simulated acoustic beam profiles of the 16-element array for beam steering and focusing at F = 12 mm and θ_s = 0° on (a) ***xy*** plane and (b) ***xz*** plane. (c) Measured beam profiles at θ_s = -45° and 45° (F = 12 mm).

in our current setup. Comparing Figs. 14 and 15, one can

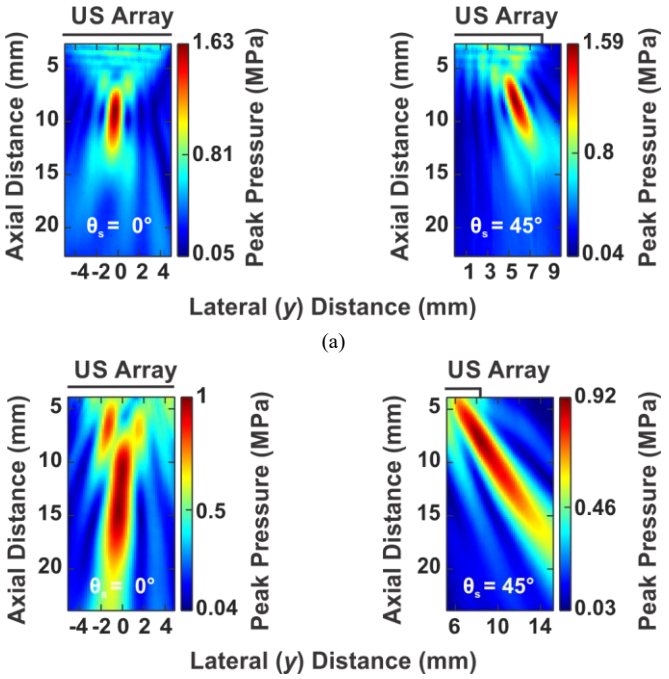

Fig. 15. Measured acoustic beam profiles for beam steering and focusing with θ_s = 0° and 45° at (a) F = 8 mm (within F_{max} = 12 mm) and (b) F = 16 mm (beyond F_{max} = 12 mm).

observe that with a fixed N and D, the shorter is the focal distance F, the smaller is the beam width (i.e., higher spatial resolution) and the higher is the peak pressure output.

To further quantify the US pressure output and spatial resolution in beam steering and focusing, the US pressure output was measured along the axial and lateral distances ($\boldsymbol{x}$ and $\boldsymbol{y}$ in Fig. 3), while steering and focusing the beam at different F of 6 mm to 18 mm and θ_s of 0º to 60º. Fig. 16a shows the measured pressure outputs along the axial distance ($\boldsymbol{y} = \boldsymbol{z} = 0$), while focusing the beam at different F (θ_s = 0°) using their corresponding delay patterns. While the spatial peak pressure was found at the expected F of 6-12 mm, it occurred at slightly shorter distances for F = 16 mm and 18 mm even with optimal delays. As F increased, the location of the peak pressure output moved to a larger axial distance, the peak pressure output decreased, and the axial beam width increased.

Fig. 16b shows similar measured pressure outputs along the lateral distance at the axial distances corresponding to the peak pressure outputs for each F in Fig. 16a. It can again be observed that as F increased, the peak pressure output decreased, and the lateral beam width increased. At F = 18 mm (well beyond F_{max} = 12 mm), the beam was barely formed, implying higher N (or D) is needed.

By steering and focusing the beam at F = 12 mm with different θ_s of 0º to 60º, the pressure outputs in parallel with the axial distance around their focal spots ($\boldsymbol{z}$ = 0 but different $\boldsymbol{y}$) were measured as shown in Fig. 16c. These results show that as θ_s increased, the peak pressure output decreased and occurred at a slightly shorter axial distance. Fig. 16d shows how the spatial peak pressure outputs (measured at the optimal axial distances in Fig. 16c) shifted and decreased along the lateral direction by increasing θ_s, which are consistent with the results

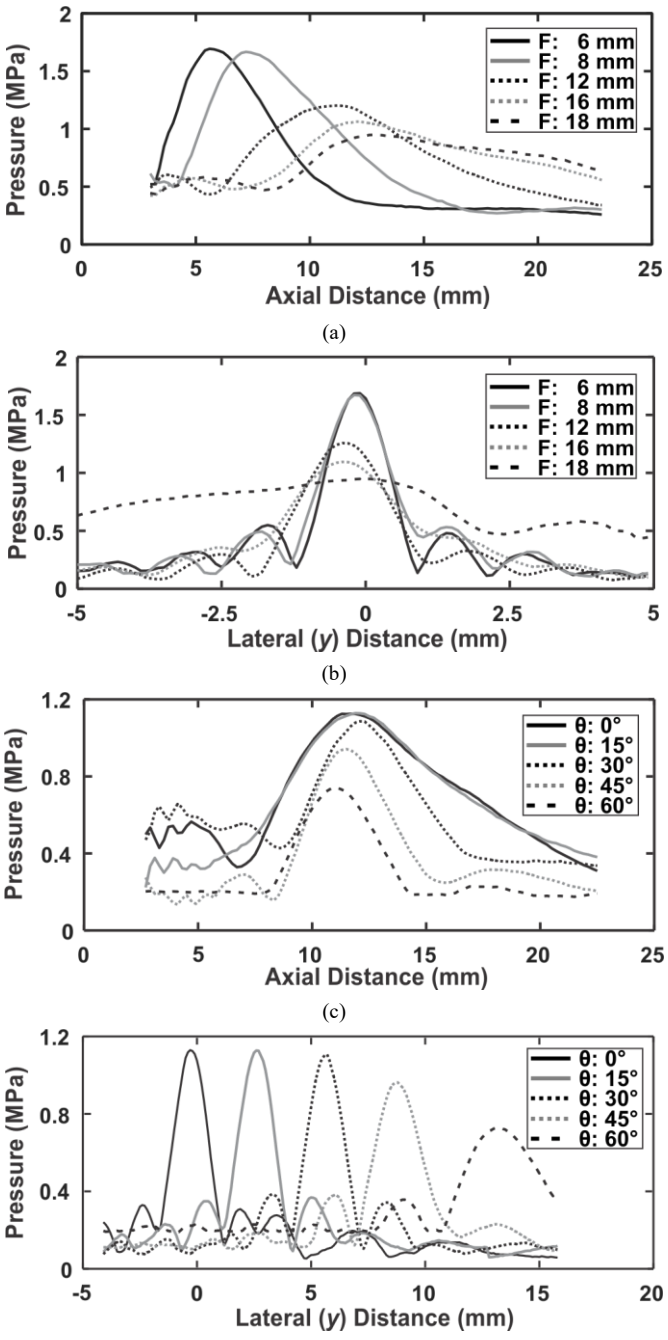

Fig. 16. Measured US pressure output in beam steering and focusing at different F and θ_s. (a) Pressure vs. axial distance at different F, (b) pressure vs. lateral distance at different F, (c) pressure vs. axial distance at different θ_s, and (d) pressure vs. lateral distance at different θ_s.

in Figs. 14 and 15. Note that the beam widths in Figs. 16c and 16d at $\theta_s \neq 0$ are not the same as axial and lateral resolution.

D. Effect of Tissue and Skull on Acoustic Beam Profile

A beam measurement was performed with a chicken tissue to mimic heterogeneity and nonlinearity presented by a tissue medium. A ~ 4.4 mm thick piece of chicken breast was wrapped around the array. The beam was focused at F = 12 mm and θ_s of 0º, and the US pressure output was measured on the $\boldsymbol{yz}$ plane. Fig. 17a shows the beam profiles with and without the chicken breast. In the presence of the chicken breast, the peak pressure

TABLE III
CHARACTERISTICS OF ULTRASOUND TRANSDUCERS AND ARRAYS FOR ULTRASOUND NEUROMODULATION APPLICATIONS

Reference	US Transducer, # Elements (N)	Transducer / Array Size (mm)	Freq., f (kHz)	Focal Distance, F (mm)	Spatial Resolution (mm)		Peak US Pressure (MPa)	US Intensity, I_{SPPA} (W/cm^2)
					Lateral	Axial		
[5]	Single PZT, 1	Diameter = 13	800	7	2.2	-	0.191	0.760
[8]	Single PZT, 1	Diameter = 16	600	10	3	11.5	0.81	20
[9]	Single PZT, 1	Diameter = 64	2000	20	1.5	8	-	8 (I_{SPTA})
[10]	Single PZT, 1	Diameter = 60	250	70	7	47	-	14.3
[11]	Single PZT, 1	Diameter = 64	320	10 - 12	4.3	33	0.6	5.1
[13]	Single, 1	Diameter = 30	500	30	4.9	18	2.5	50
[14]	Single, 1	-	270	30	3	17	1.5	16.6
[16]	Single PZT, 1	Diameter = 5	2000	7	1.2	-	1.2	46
[19]	Ring CMUT, 32	Diameter = 8.1	183	2.3	2.75	-	0.052	0.530
[20]	1D PZT, 128	20×5	5000	50	1.7	-	1.1	-
[21]	2D Sm-PMN, 16×16	17.5×17.5	1000	15	1.95	3.14	1.28	-
[22]	2D PZT, 26×26	5×4	8400	5	0.215	1.68	0.1	-
[23]	2D CMUT, 32×32	8×8	2000	5	0.4	2.4	0.575	12.4
This Work	**1D PZT, 16**	**16.7×7.7**	**833.3**	**12**	**1.6**	**9**	**1.15**	**32.1**

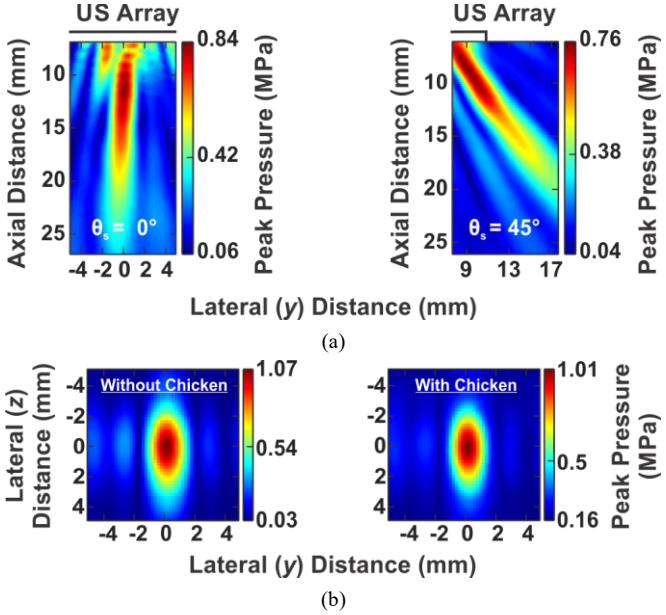

Fig. 17. Measured acoustic beam profiles for beam steering and focusing at (a) F = 16 mm and θ_s = 0° and 45° on ***xy*** plane in the presence of a rat skull, as shown in the Fig. 10 inset, and (b) F = 12 mm and θ_s = 0° on the ***yz*** plane in the presence of the chicken breast tissue.

slightly reduced by 5.6%, while the lateral resolution in ***y*** and ***z*** directions remained almost the same at 1.4 mm and 3.4 mm, respectively.

A rat skull was introduced between the US array and the hydrophone to mimic a more realistic experimental setup. The ~ 0.6 mm thick skull was placed 2 mm away from the array surface. The beam was focused at F = 16 mm with θ_s of 0° and 45°, and the US pressure output was measured, as shown in Fig. 17b. The spatial peak pressure outputs were 0.84 MPa and 0.76 MPa at θ_s of 0° and 45°, respectively. The measured axial and lateral resolutions at θ_s = 0° were 7.2 mm and 1.6 mm, respectively. It is worth noting that F = 16 mm was chosen for skull measurements (unlike F_{max} = 12 mm) to avoid any impact of the hydrophone to the skull. Also, the curved shape of the skull refrained us from getting very close to the array, resulting in a truncated beam profile at θ_s of 45°.

Comparing Fig. 17b with Fig. 15b (without skull), several lessons can be learned from introducing the skull. 1) The beam shape was distorted for both θ_s of 0° and 45°. 2) The peak pressure output occurred closer to the array (11.6 vs. 16.2 mm at θ_s = 0°), and as the possible consequence the axial and lateral resolutions were improved by 30.7% (7.2 vs. 10.4 mm) and 20% (1.6 vs. 2 mm) at θ_s = 0°, respectively (they also improved at θ_s = 45°). These changes could be due to the skull curvature, acting as a lens. 3) The spatial peak pressure output reduced by 16% (0.84 vs. 1 MPa) and 17.4% (0.76 vs. 0.92 MPa) for θ_s of 0° and 45°, respectively. These variations could be attributed to the high acoustic attenuation, reflections due to acoustic impedance mismatch, and phase aberrations introduced by the skull. In future, matching layers can be used to achieve acoustic impedance matching [17], [37].

Table III compares the characteristics of state-of-the-art US transducers and arrays with our fabricated array for USN applications. Most prior works have utilized a bulky single-element transducer with a large focal spot. Our fabricated 16-element array operates at 833.3 kHz and achieves a high peak pressure of 1.15 MPa at a focal distance of 12 mm with lateral and axial resolutions of 1.6 mm and 9 mm, respectively. The maximum I_{SPPA} and mechanical index in our measurements were 65.9 W/cm^2 and 1.8 (for the focused beam at F = 8 mm, θ_s = 0°), which are within the FDA safety limits of 190 W/cm^2 and 1.9, respectively [38]. The transducers in Table III with comparable spatial resolution and US pressure output have successfully and safely stimulated neural tissue.

V. CONCLUSION

A design methodology was proposed for the optimization of a US phased array by maximizing a FoM (considering both power efficiency and spatial resolution of an array) and minimizing a directivity function (attenuating side/grating lobes) for USN applications. For an intended tissue volume and sonication frequency (f), the proposed procedure helps designers identify the optimal geometry of an array, including US elements' width, length, and thickness, as well as array's aperture, interelement spacing, and number of elements. As an example, a linear 16-element array for USN of a rat's brain was optimized, fabricated, and characterized using a 16-channel

commercially available driver board. The operation of the array in beam steering and focusing at f = 833.3 kHz with high acoustic pressure output at different focal distances (6-18 mm) and steering angles (0-60°) was demonstrated in measurements inside a water tank. The effect of a rat skull on the acoustic beam profile was also measured and discussed.

This work presented an optimized US phased array that considers design settings imposed by the application and fabrication constraints for USN applications. In future, we plan to 1) apply phase corrections to mitigate skull effects, 2) conduct *in vivo* experiments with stimulating different brain regions on and off the normal axis through beam focusing and steering (no mechanical movement), and 3) develop an efficient CMOS ASIC and integrate it with the US array to realize a fully wearable USN system.

REFERENCES

[1] W. Tyler, Y. Tufail, M. Finsterwald, M. Tauchmann, E. Olson, and C. Majestic, "Remote excitation of neuronal circuits using low-intensity, low-frequency ultrasound," *Plos One*, vol. 3, Oct. 2008.

[2] T. Wagner, A. Valero-Cabre, and A. Pascual-Leone, "Noninvasive human brain stimulation," *Ann. Rev. Biomed. Eng.*, pp. 527–565, 2007.

[3] K. Abe and T. Taira, "Focused ultrasound treatment, present and future," *Neurol. Med. Chir*, vol. 57, pp. 386-391, Aug. 2017.

[4] A. Bystritsky and A. Korb, "A review of low-intensity transcranial focused ultrasound for clinical applications," *Curr. Behav. Neurosci. Rep.*, vol. 2, pp. 60-66, Mar. 2015.

[5] H. Zhou, L. Niu, X. Xia, Z. Lin, X. Liu, M. Su, R. Guo, L. Meng, and H. Zheng, "Wearable ultrasound improves motor function in an MPTP mouse model of Parkinson's disease," *IEEE Trans. Biomed. Eng.*, vol. 66, pp. 3006-3013, Nov. 2019.

[6] D. S. Hersh and H. M. Eisenberg, "Current and future uses of transcranial focused ultrasound in neurosurgery," *J Neurosurg Sci.*, vol. 62, pp. 203-213, Nov. 2017.

[7] Y. Tufail, A. Yoshihiro, S. Pati, M. Li, and W. Tyler, "Ultrasonic neuromodulation by brain stimulation with transcranial ultrasound," *Nature Protocols*, vol. 6, no. 9, pp. 1453-1470, 2011.

[8] W. Lee, P. Croce, R. Margolin, A. Cammalleri, K. Yoon, and S. Yoo, "Transcranial focused ultrasound stimulation of motor cortical areas in freely-moving awake rats," *BMC Neuroscience*, vol. 19, pp. 57, Sep. 2018.

[9] E. Mehic, J. Xu, C. Caler, N. Coulson, C. Moritz, and P. Mourad, "Increased anatomical specificity of neuromodulation via modulated focused ultrasound," *PLOS One*, vol. 9, Feb. 2014.

[10] W. Lee, S. Lee, M. Park, L. Foley, E. Purcell, H. Kim, K. Fischer, L. Maeng, and S. Yoo, "Image-guided focused ultrasound–mediated regional brain stimulation in sheep," *Ultrasound Med. Biol.*, vol. 42, pp. 459-470, 2016.

[11] T. Deffieux, Y. Younan, N. Wattiez, M. Tanter, P. Pouget, and J. Aubry, "Low-intensity focused ultrasound modulates monkey visuomotor behavior," *Current Biology*, vol. 23, pp. 2430–2433, Dec. 2013.

[12] W. Legon, A. Rowlands, A. Opitz, T. Sato, and W. Tyler, "Pulsed ultrasound differentially stimulates somatosensory circuits in humans as indicated by EEG and fMRI," *PLOS One*, vol. 7, Dec. 2012.

[13] W. Legon, T. Sato, A. Opitz, J. Mueller, A. Barbour, A. Williams, and W. Tyler, "Transcranial focused ultrasound modulates the activity of primary somatosensory cortex in humans," *Nature Neurosci.*, vol. 17, pp. 322-333, Feb. 2014.

[14] W. Lee, H. Kim, Y. Jung, Y. Chung, I. Song, J. Lee, and S. Yoo, "Transcranial focused ultrasound stimulation of human primary visual cortex," *Scien. Reports*, vol. 6, pp. 1-12, Sep. 2016.

[15] X. Niu, K. Yu, and B. He, "On the neuromodulatory pathways of the in vivo brain by means of transcranial focused ultrasound," *Current Opinion Biomed. Eng.*, vol. 8, pp. 61–69, 2018.

[16] G. Li, W. Qiu, Z. Zhang, Q. Jiang, M. Su, R. Cai, Y. Li, F. Cai, Z. Deng, D. Xu, and H. Zhang, "Noninvasive ultrasonic neuromodulation in freely moving mice," *IEEE Tran. Biomed. Eng*., vol. 66, no. 1, pp. 217-224, Jan. 2019.

[17] H. Sadeghi Gougheri, A. Dangi, S. Kothapalli, and M. Kiani, "A Comprehensive study of ultrasound transducer characteristics in microscopic ultrasound neuromodulation," *IEEE Trans. Biomed. Cir. Syst.*, vol. 13, pp. 835-847, Oct. 2019.

[18] V. Pashaei, P. Dehghanzadeh, G. Enwia, M. Bayat, S. Majerus, and S. Mandal, "Flexible body-conformal ultrasound patches for image-guided neuromodulation," *IEEE Trans. Biomed. Cir. Syst.*, vol. 14, no. 2, pp. 305-318, Apr. 2020.

[19] H. Kim, S. Kim, N. Sim, C. Pasquinelli, A. Thielscher, J. Lee, and H. Lee, "Miniature ultrasound ring array transducers for transcranial ultrasound neuromodulation of freely-moving small animals," *Brain Stim.,* vol. 12, pp. 251-255, Mar. 2019.

[20] G. Li, W. Qiu, J. Hong, Q. Jiang, M. Su, P. Mu, G. Yang, Y. Li, C. Wang, H. Zhang, and H. Zheng, "Imaging-guided dual-target neuromodulation of the mouse brain using array ultrasound," *IEEE Trans. Ultras. Ferroel. Freq. Cont.,* vol. 65, pp. 1583-1589, Sept. 2018.

[21] Z. Zhang, M. Su, F. Li, R. Liu, R. Cai, G. Li, Q. Jiang, H. Zhong, T. Shrout, S. Zhang, H. Zheng, and W. Qiu, "New Sm-PMN-PT ceramic-based 2-D array for low-intensity ultrasound therapy application," *IEEE Trans. Ultras. Ferroel. Freq. Cont.*, vol. 67, pp. 2085-2094, Oct. 2020.

[22] T. Costa, C. Shi, K. Tien, J. Elloian, F. Cardoso and K. Shepard, "An integrated 2D ultrasound phased array transmitter in CMOS with pixel pitch-matched beamforming," *IEEE Trans. Biomed. Cir. Syst.*, vol. 15, pp. 731-742, Aug. 2021.

[23] C. Seok, O. Adelegan, A. Biliroğlu, F.Yamaner, and Ö.Oralkan, "A wearable ultrasonic neurostimulator—part II: A 2D CMUT phased array system with a flip-chip bonded ASIC," *IEEE Trans. Biomed. Cir. Syst.*, vol. 15, pp. 705-718, Aug. 2021.

[24] O. Von Ramm and S. Smith, "Beam steering with linear arrays," *IEEE Trans. Biomed. Eng.,* vol. BME-30, pp. 438-452, Aug. 1983.

[25] S. Wooh and Y. Shi, "Optimum beam steering of linear phased arrays," *Wave Motion,* vol. 29, pp. 245-265, Apr. 1999.

[26] S. Edelman, "Understanding ultrasound physics," E.S.P Ultrasound 4 edition, July 2012.

[27] B. Treeby and B. Cox, "k-Wave: MATLAB toolbox for the simulation and reconstruction of photoacoustic wave fields," *J. Biomed. Opt.,* Apr. 2010.

[28] E. Martin, J. Jaros, and B. Treeby, "Experimental validation of k-Wave: nonlinear wave propagation in layered, absorbing fluid media," *IEEE Trans. Ultras. Ferroelect. Freq. Contr*., vol. 67, pp. 81-91, Jan. 2020.

[29] C. Poelma, "Ultrasound imaging velocimetry: a review," *Experiments in Fluids,* vol. 58, p. 3, Dec. 2016.

[30] T. Mast, "Empirical relationships between acoustic parameters in human soft tissues," *Acoust. Res. Letter Online,* vol. 1, Nov. 2000.

[31] H. Kim, A. Chiu, S. Lee, K. Fischer, and S. Yoo, "Focused ultrasound-mediated non-invasive brain stimulation: examination of sonication Tparameters," *Brain Stimulation*, vol. 7, pp.748-756, Sep. 2014.

[32] G. Paxinos and C. Watson, *The rat brain in stereotaxic coordinates: hard cover edition*: Elsevier, 2006.

[33] Y. Igarashi, S. Kajiyama, Y. Katsube, T. Nishimoto, T. Nakagawa, Y. Okuma, Y. Nakamura, T. Terada, T. Yamawaki, T. Yazaki, Y. Hayashi, K. Amino, T. Kaneko, and H. Tanaka, "Single-chip 3072-element-channel transceiver/128-subarray-channel 2-D array IC with analog RX and all-digital TX beamformer for echocardiography," *IEEE J. Solid-State Cir.*, vol. 54, pp. 2555-2567, Sep. 2019.

[34] M. Meng, and M. Kiani, "Design and optimization of ultrasonic wireless power transmission links for millimeter-sized biomedical implants," *IEEE Trans. Biomed. Cir. Syst*., vol. 11, no. 1, pp. 98–107, Feb. 2016.

[35] A. Gefen, Q. Gefen, N Fau, Q. Zhu, R. Raghupathi, and S. Margulies, "Age-dependent changes in material properties of the brain and braincase of the rat," *J Neurotrauma,* vol. 20, pp. 1163-1177, Nov. 2003.

[36] P. Tsai, H. Sadeghi Gougheri, and M. Kiani, "Skull impact on the ultrasound beam profile of transcranial focused ultrasound stimulation," *41st IEEE Eng. Medicine Biology Conf.*, pp. 1-4, July 2019.

[37] D. Callens, C. Bruneel, and J. Assaad, "Matching ultrasonic transducer using two matching layers where one of them is glue," *NDT & E. Int.*, vol. 37, pp. 591-596, Dec. 2004.

[38] F. Duck, "Medical and non-medical protection standards for ultrasound and infrasound," *Prog. in Biophys. Bioeng.,* vol. 93, pp. 176-191, Apr. 2007.